Key Point:
- A simple conceptual model combining fracturing and pressure solution can explain compaction creep

Correspondence to:
D. Keszthelyi,
danielke@fys.uio.no

First principles model of carbonate compaction creep

Daniel Keszthelyi[1], Dag Kristian Dysthe[1], and Bjørn Jamtveit[1]

[1]Physics of Geological Processes, Department of Physics and Department of Geosciences, University of Oslo, Oslo, Norway

Abstract Rocks under compressional stress conditions are subject to long-term creep deformation. From first principles we develop a simple micromechanical model of creep in rocks under compressional stress that combines microscopic fracturing and pressure solution. This model was then upscaled by a statistical mechanical approach to predict strain rate at core and reservoir scale. The model uses no fitting parameter and has few input parameters: effective stress, temperature, water saturation porosity, and material parameters. Material parameters are porosity, pore size distribution, Young's modulus, interfacial energy of wet calcite, the dissolution, and precipitation rates of calcite, and the diffusion rate of calcium carbonate, all of which are independently measurable without performing any type of deformation or creep test. Existing long-term creep experiments were used to test the model which successfully predicts the magnitude of the resulting strain rate under very different effective stress, temperature, and water saturation conditions. The model was used to predict the observed compaction of a producing chalk reservoir.

1. Introduction

Since the classical experiments of *Phillips* [1905] and *Andrade* [1910], considerable interest has focused on creep mechanism, the long-term slow deformation of materials at constant stress conditions. Following the first experiment of *Griggs* [1936] on Solenhofen limestones, numerous creep experiments were conducted on rock samples and polycrystalline materials. Creep in polycrystalline aggregates usually evolves through three stages: an initial transient phase with decelerating strain rate, a second steady state creep, and a final accelerating creep. At the low-temperature conditions of most sedimentary basins, the initial transient creep stage dominates the compaction history of porous sedimentary rocks. However, existing creep models mainly focus on the steady state creep stage of materials subject to relatively high temperatures.

Attempts to describe the transient creep includes the general exhaustion and the similar redistribution theory [*Carter and Kirby*, 1978] which describes materials as a set of elements in which stress fluctuations can cause plastic deformation. As one element is deformed, it becomes impossible (exhaustion theory) or more difficult (redistribution theory) to deform, resulting in a logarithmic overall strain in time. Although the model works well on selected examples, it ignores the underlying microstructural phenomena of the creep mechanism.

A series of micromechanical models was created to describe creep at low stresses and low temperatures as a result of underlying fracturing process for given pore configurations [e.g., *Ashby and Sammis*, 1990; *Brantut et al.*, 2012]. *Brantut et al.* [2012] identified the different phases of the creep process as characteristic fracturing steps: i.e., transient creep as the decelerating stage of subcritical crack growth, accelerating creep as a consequence of crack interactions, and the apparent "steady state creep" as the stage when subcritical fracture growth is near its minimum slowest speed.

Besides subcritical fracture growth, pore collapse is also associated to compaction. *Zhu et al.* [2010] describe the phenomenon as a plastic deformation localized around large pores triggered by hydrostatical stresses. *Vajdova et al.* [2012] carried out microstructural analysis on samples compacted in a dry environment and found evidence of microscopic fracturing when shear stresses were present and found pore collapse in case of hydrostatic stresses.

Another phenomenon associated with compaction creep is pressure solution: the dissolution of minerals in regions at high stress (e.g., grain contacts) and the precipitation to areas with lower stresses (see review by *Gratier et al.* [2013]). Pressure solution has been identified under both high and low stress and temperature

conditions [e.g., *Renard et al.*, 1999; *Croize et al.*, 2013]. However, in models, it is commonly regarded as becoming an important process only at high stresses (i.e., with increasing depth in the crust [e.g., *Brantut et al.*, 2012]). *Brantut et al.* [2014] carried out experiments on wet limestone samples and found that microstructural fracturing cannot explain deformation at lower strain rates and mentioned pressure solution as a candidate for the creep mechanism.

Here we present an alternative micromechanical approach to describe transient creep of wet crustal rocks by combining fracturing and pressure solution in fluid-filled porous rocks. We use a statistical mechanical approach for upscaling and predict strain rate at reservoir scale. The model is tested against existing triaxial creep experiments and compaction data from a subsiding producing reservoir. We find good agreement between measured and theoretical values.

2. Model Description

We consider deformations in the long-term, and we base our model on the compaction model proposed by *Japsen et al.* [2011] for chalk samples, and we make the following main assumptions:

1. At low stresses a rock is a nonreactive, elastic solid with a collection of "material flaws." These flaws are the pores inside the rock, and they have a probability distribution, $p(r)$ of pore radii r.
2. Crustal rocks at a certain depth are subject to a maximum σ_1 and a minimum σ_3 principal stress and pore fluid pressure, p. This model assumes that deformation is controlled by the maximum principal effective stress, which in the simplest case equals $\sigma_e = \sigma_1 - p$ [*Terzaghi*, 1943].
3. When the effective stress exceeds a threshold, fractures will start to propagate from all pores of radius $r > \gamma E / \sigma_e^2$ (where E is the Young's modulus and γ is the interfacial energy of the rock-pore fluid surface). This can happen either by shearing or by local perturbations caused by eventual pore collapse.
4. The number of fractures created is proportional to the number of pores involved in the fracturing process. The fracture density ρ_f describes the abundance of these fractures.
5. Fracturing is instantaneous, and for long-term deformations we neglect elastic strain, and strain due to the formation of fractures and due to pore collapse.
6. The new fractures are reactive sites where pressure solution takes place if there is water present. In the simplest case the fraction of water-wet fractures equals the water saturation S_w of the rock.
7. The rate of pressure solution at each reactive site is a function of effective stress and the initial porosity only. This means that it represents a viscous strain where the viscosity is porosity dependent.
8. Only short time and low strains are considered in this first version of the model. No evolution with time of pressure solution rate, pore size distribution, or porosity is considered here. This implies that strain rate evolution is a function of the effective stress evolution only.

2.1. Model Details

The proposed micromechanical model is composed of the following steps: Effective stress increase causes microstructural fracturing starting from pores larger than a given threshold (either by shear fracturing or by perturbation related to pore collapse). This is followed by subsequent pressure solution on the freshly created fracture surfaces. This model is a first step toward a complete model for time-dependent deformation of wet rocks and many gross simplifications are made to keep the model predictive and with no free fitting parameters. The first simplification is to consider only the maximum principal stress of the rock during compaction. This amounts in some sense to a vertical (and not curved/shear enhanced) end cap in the Mohr-Coloumb diagram of rock failure [*Schutjens et al.*, 2004].

2.1.1. Fracture Propagation

In the Griffith concept of materials, cracks can initiate from inhomogeneities and propagate throughout the material [*Griffith*, 1921; *Irwin*, 1958; *Ashby and Sammis*, 1990]. Such inhomogeneities can be pores or phases which have different mechanical properties from the rest of the rock matrix, and they may act as a source for fractures (see Figure 1a).

The crack growth rate (also referred to as propagation rate) is a function of the energy release rate G (the mechanical energy released for an incremental crack extension) which, given a shape and position of the initial flaw, depends only on the load stresses [*Røyne et al.*, 2011; *Lawn*, 1993].
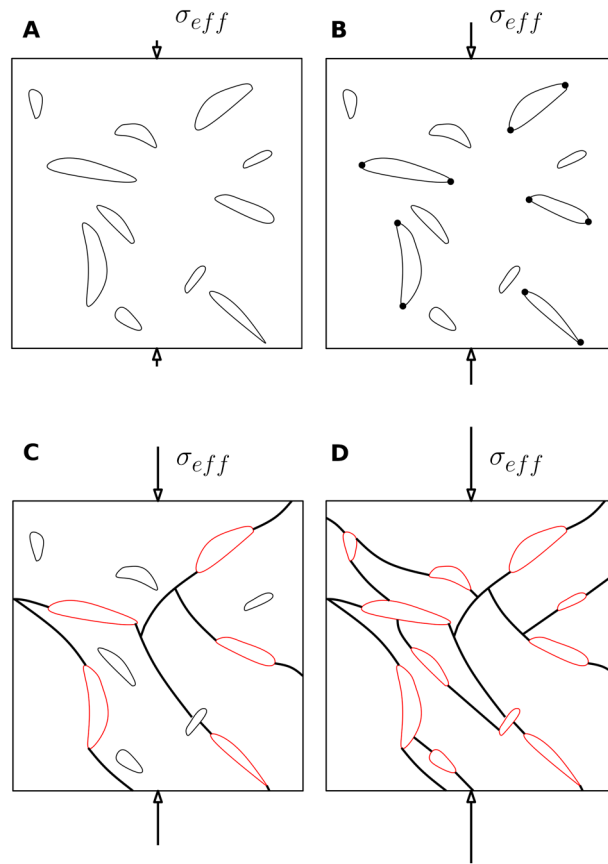
Figure 1. The development of fractures inside a rock sample with increasing effective stress. (a) Initially, the untouched rock contains a set of pores inside the rock matrix matrix. (b) With increasing effective stress first fractures initiate at the largest pores and they propagate inside the chalk matrix until (c) they reach other fractures (coalescence). (d) If effective stress is large enough, smaller pores will be involved in the fracturing process.

Consider elastic energy U_E stored in a material under a far-field effective stress σ_e around a fracture having a characteristic length scale r. The elastic energy release rate $G = \partial U_E / \partial r$ as the fracture length is increased from r to $r + \partial r$ scales as

$$G \propto \frac{\sigma_e^2 r}{E},$$ (1)

where E is the Young's modulus.

The fracture can only propagate if the elastic energy gained is larger than the surface energy created (U_s):

$$G = \frac{\partial U_E}{\partial x} \geq \frac{\partial U_s}{\partial x} = 2\gamma_s,$$ (2)

where γ_s is the surface energy of the solid. *Røyne et al.* [2011] measured the surface energy of calcite for various oil-water mixtures. Their results may be summarized in a simple linear relation depending on the water saturation S_w:

$$\gamma_s = S_w \times 0.15 + (1 - S_w) \times 0.32 \text{ J/m}^2.$$ (3)

Thus, we have a criterion for slow propagation of fractures:

$$\sigma_e \geq \sqrt{\frac{2\gamma_s E}{r_{max}}} = \frac{\sqrt{2 \cdot 12.9 \text{ GPa} \cdot (0.32 - 0.17 \cdot S_w) \text{ J/m}^2}}{\sqrt{r_{max}}} = \frac{91.5 - 29 \cdot S_w \text{ MPa} \cdot \mu\text{m}^{1/2}}{\sqrt{r_{max}}}.$$ (4)

We have not included geometry-dependent prefactors as this will vary widely inside the material.

This in turn means that the largest pores are subject to fracture initiation before the smaller pores. As the effective stress increases, smaller and smaller pores will be involved in the fracturing process. A series of figures illustrating the development of fractures is shown in Figure 1.

Once initiated, cracks can grow larger if stresses are large enough (see Figure 1b) [*Ashby and Sammis*, 1990; *Lawn*, 1993]. Eventually, they start to interact with each other and form a coherent fracture as shown in Figures 1c and 1d. According to *Ashby and Sammis* [1990], in compressional settings with crack growth, the energy release rate is decreasing and crack growth can eventually stop without stress increase or interaction with other pores. In wet rocks, however, there are two mechanisms that can help further propagation of fractures: stress corrosion and pressure solution. The model of *Brantut et al.* [2012, 2013] mentioned the effect of stress corrosion—the rock fluid reactions that occur between the pore fluid and the strained atomic bonds close to the fracture tip and which weakens the area around the fracture tip facilitating the growth of the fracture even without stress increase or interactions. Pressure solution may also reduce normal stress on fractures and therefore increase stress in the rock around and keep the energy release rate large enough to propagate the fractures. While this question is not well studied, there is evidence that pressure solution can smooth out rough surfaces in the presence of shear stresses [*Bos et al.*, 2000], and if this is happening in the initial segment of a growing fracture, stress concentration can be increased at the fracture tip. Furthermore, *Gratier et al.* [1999] showed experimental evidence of fracturing occurring during pressure solution. These arguments suggest that subcritical fracture growth and the growth of a fracture network once cracks are initiated is possible in carbonate rocks and will be further facilitated by coalescence by the small spacing between pores (as in North Sea chalk).

Using backscattered electron (BSE) images of chalk samples from the Ekofisk field (presented in *Japsen et al.* [2011]), we estimated that the characteristic distance between pores is below 100 μm and typically in the range of the grain sizes (1–10 μm). According to the model, this is the characteristic length scale of new fractures; thus, for extremely slow fracture propagation rates of 10^{-10} m/s, it takes only between several hours and 10 days to propagate a fracture between existing pores. Since the fracture propagation speed is a sharp function of the energy release rate G, the main damage contribution comes from the fractures which propagate on a second to hours timescale. Thus, we will not consider fracture propagation as a rate-limiting process in this model; i.e., fracturing is assumed to be instantaneous.

2.1.2. Pressure Solution on the New Reactive Fracture Surfaces

We consider that rocks do not creep until stressed to the point of failure as described in the last section. This means that they are unreactive and do not undergo pressure solution. This may be because all grain boundaries/contacts are solid-solid contacts with no water film that promotes pressure solution [*Gratier et al.*, 2013] or because dissolution-precipitation processes are stopped by organic matter coating the grain surfaces [*Hassenkam et al.*, 2009, 2011].

Grain boundary healing [*Hickman and Evans*, 1995; *Gratier et al.*, 2013] and cementation [*Moore*, 1989] are two of the main processes that give sedimentary rocks cohesive strength. In a healed and/or cemented grain contact there is no water present to mediate pressure solution. This hinders the healed and cemented rock from creeping until distributed damage in the form of pervasive microfracturing creates new reactive surface area where pressure solution may occur.

In chalk, a calcitic rock of biogenic origin, it has been found that the calcite mineral grains are coated by organic material that was clearly identified by *Hassenkam et al.* [2009, 2011]. *Japsen et al.* [2011] showed that this coating that renders the rock unreactive had consequences for the compaction of the chalk during burial: The rock would only compact when fresh surface area was created by increased burial depth triggering fracturing. Pressure solution takes place only if fracturing initiates; pore fluid enters the new fractures and is associated with dissolution of calcite along the new fracture surfaces and precipitation at sites where chemical potential is lower, mainly inside the pore space. The transport of material to the pores is by diffusion along the thin fluid film (Figure 2) inside the fracture.

Calcite dissolution/precipitation in water can be described by the following simplifed chemical reaction:

$$CaCO_{3,\,(s)} + H_2CO_{3\,(l)} \Longleftrightarrow Ca^{2+}_{(aq)} + 2HCO^-_{3,\,(aq)}, \tag{5}$$

where the equilibrium between reactants and the products is controlled by temperature and stress conditions and by the chemical composition of the aqueous solution.
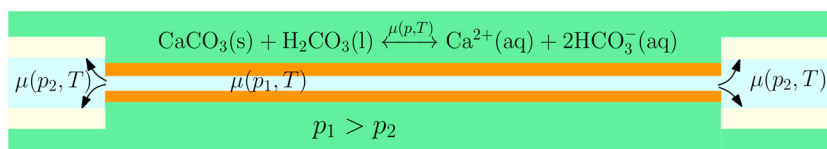
Figure 2. Pressure solution of calcite: Calcite dissolves along grain contacts where stresses and hence the chemical potential of calcite are locally higher, and after diffusion it precipitates inside areas where chemical potential is lower. The effect is that grain contact areas increase, and therefore, the distance between grains decreases. A review of the pressure solution process can be seen in *Gratier et al.* [2013] and *Pluymakers et al.* [2014].

Pressure solution causes grains to approach each other along dissolution surfaces. The total strain rate by pressure solution $\dot{\epsilon}$ is the product of the pressure dissolution rate $\dot{\xi}$ at each individual interface, the water saturation S_w, and the number of such interfaces per unit length, $\rho_f(\sigma_e)$, normal to the effective stress direction.

$$\dot{\epsilon} = S_w \rho_f \dot{\xi}. \tag{6}$$

For comparison, most pressure solution experiments are performed on aggregates. Equation (6) applies to the total strain rate of compaction of aggregates of grains of mean size d with

$$\rho_{f,\text{aggr}} = 1/d. \tag{7}$$

In our model $\rho_f(\sigma_e)$ is the fracture density (see Figure 3 and section 2.1.3).

In this simplified relation pressure solution rate ($\dot{\xi}$) is defined as the speed with which the two dissolution surfaces are approaching each other.

To estimate the pressure solution rate, we use the most thorough study of calcite pressure solution creep performed by *Zhang et al.* [2010]. Their experiments were performed on ground limestone (96% calcite), analytical grade, or ultrapure calcite powder of varying grain sizes (12–82 μm). They parametrize their results in models for pressure solution creep limited by precipitation, dissolution, and diffusion. The model parameters are fitted to the initial phase (typically the first 5–20 h of 100 to 800 h experiments).

All experiments showed significant decrease of strain rate toward the end of the experiments, with strain rates typically 1–3 orders of magnitude lower than the model. This was explained by the fact that at low strains
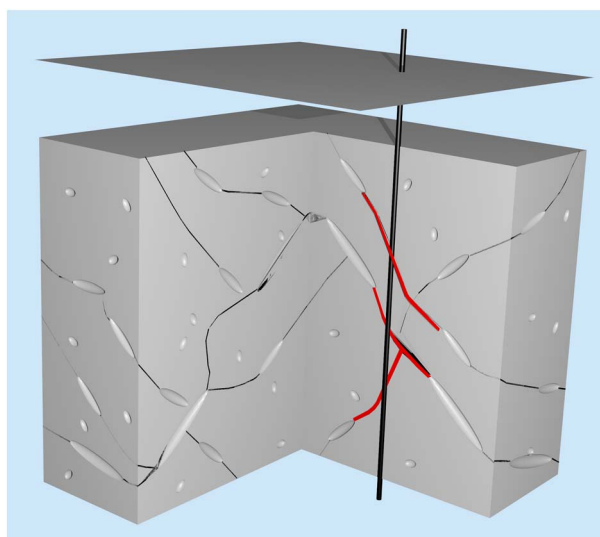

Figure 3. Model of a rock sample subject to effective stress σ_{eff}. Pores larger than a certain length $l(\sigma_e)$ will close (see equation (4)). Between the pores fresh fracture surface is forming during microcracking. These surfaces are the site for the pressure solution process. The total strain rate by pressure solution is the product of the dissolution rate along individual fractures, and the fracture density is the expected number of fractures (i.e., pressure solution sites) by unit length along an arbitrary vertical unit line. An arbitrary vertical line is drawn in black; the crossed fractures are in red.

(i.e., at high porosity) pressure solution is diffusion controlled, while at higher stresses (i.e., at lower porosity) the growing impurity content in the pore fluid inhibiting precipitation slows down the pressure solution. Furthermore, the comparison of strain rates between the limestone, analytical grade, and ultrapure calcite shows that pressure solution creep is very quickly slowed down by trace amounts of impurities. The conclusion we draw is that for carbonates pressure solution can be either reaction controlled or diffusion controlled and for simplicity we choose always the slowest of these in the calculations using the original porosity values to determine pressure solution rate. Modeling the time-dependent effect of the slowing down pressure solution creep is outside the scope of this paper, and we consider two different pressure solution rates.

The first approach to calculate pressure solution rate is following a theoretical model based on *Zhang et al.* [2010] and *Pluymakers et al.* [2014]. They were assuming a simple cubic packing of spherical grains and pressure solution happening on all six possible grain contacts for each grain. Using their model pressure dissolution rate, $\dot{\xi}_p$ can be calculated in the precipitation limited case as

$$\dot{\xi}_p = A_p k_p \Omega \left[\exp\left(\frac{\sigma_e \Omega}{RT} \frac{Z}{\pi} \frac{q}{q-2\phi} \right) - 1 \right] \frac{2\phi}{q-2\phi} \tag{8}$$

and in the diffusion limited case pressure dissolution rate $\dot{\xi}_d$ is

$$\dot{\xi}_d = \frac{2\pi \cdot A_c DCSZ}{\beta F d^2} \left[\exp\left(\frac{\sigma_e \Omega}{RT} \frac{Z}{\pi} \frac{q}{q-2\phi} \right) - 1 \right] \left(\frac{q}{q-2\phi} \right), \tag{9}$$

where k_p is the temperature-dependent rate coefficients for precipitation; β, A_p, and A_c are geometric constants; σ_e is the effective stress; ϕ is the porosity; d is the diffusion distance taken equal to the mean pore size; Ω is the molar volume of calcite; D is the diffusivity of ions within the grain boundary fluid; C is the solubility of the solid; S is the mean thickness of the grain boundary fluid phase; R is the gas constant; T is temperature; Z is the coordination number; F is the grain shape factor; and $q = 2\phi_0 = 0.9528$, where $\phi_0 = 1 - \pi/6$ is the porosity of simple cubic packing of spheres. By unifying all the dimensionless constants, the two relations can be rewritten as

$$\dot{\xi}_p = B k_p \Omega \left[\exp\left(\frac{\sigma_e \Omega}{RT} f(\phi) \right) - 1 \right] \phi f(\phi), \tag{10}$$

where $B = 2A_p \exp(Zq/\pi) = 26.91$ and $f(\phi) = 1/(q-2)\phi$ and

$$\dot{\xi}_d = MDCS \frac{1}{d^2} \left[\exp\left(\frac{\sigma_e \Omega}{RT} f(\phi) \right) - 1 \right] f(\phi), \tag{11}$$

where $M = A_c Z \exp(Zq/\pi)/(\beta F) = 34.27$. The rate coefficient for precipitation is calculated as

$$k_p = k_{p,0} \exp\left(-\frac{Q_p}{RT} \right) \quad \text{where} \quad k_p = 10^{-10} \text{ m/s at } T = 25°C, \tag{12}$$

the diffusion constant D is

$$D = D_0 \exp\left(-\frac{Q_d}{RT} \right) \quad \text{where} \quad D = 10^{-10} \text{ m}^2/\text{s at } T = 25°C, \tag{13}$$

where Q_p and Q_s are activation energy constants. The solubility C of calcite (a dimensionless number) has the temperature dependence [*Zhang et al.*, 2010]:

$$\log\left(C^2 \right) = -171.9065 - 0.077993 \frac{1}{K} T + \frac{2839.319K}{T} + 71.595 \log(T). \tag{14}$$

Other parameters are constant and shown in Table 1.

Equations (10) and (11) depend only on three external parameters: porosity ϕ, temperature T, and effective stress σ_e; the other parameters are kept constant in this study. The effect of impurities are neglected since the ion composition of the samples are not known and a significant part of the North Sea chalk formation is

Table 1. Internal Parameters Used in the Pressure Solution Model

Symbol	Definition	Used Value	Source
A_c	Geometric constant	4	*Pluymakers et al.* [2014]
A_p	Geometric constant	4	*Pluymakers et al.* [2014]
S	Grain boundary thickness	$2 \cdot 10^{-10}$ m	*Zhang et al.* [2010]
Z	Coordination number	4	*Pluymakers et al.* [2014]
β	Geometric factor	0.5	*Pluymakers et al.* [2014]
F	Grain shape factor	π	*Pluymakers et al.* [2014]
d	Diffusion distance		Taken equal to the average pore diameter
Ω	Molar volume of calcite	$3.692 \cdot 10^{-5}$ m^3/mol	*Zhang et al.* [2010]
R	Universal gas constant	8.314 J $\cdot$ mol$^{-1} \cdot$ K^{-1}	
Q_p	Activation energy	$46,000$ J $\cdot$ mol^{-1}	*Zhang et al.* [2010]
Q_d	Activation energy	$33,000$ J $\cdot$ mol^{-1}	*Zhang et al.* [2010]
D_0	Diffusion constant	$1.63 \cdot 10^{-16}$ m$^2 \cdot$ s^{-1}	From equation (13) and *Zhang et al.* [2010]
$k_{p,0}$	Rate constant of precipitation at $T = 0$ K	0.01167 m $\cdot$ s^{-1}	From equation (12) and *Zhang et al.* [2010]

composed of chalk with low-magnesium content [*Feazel*, 1988] which indicates that this is a valid assumptions for the samples of the *Omdal et al.* [2010] experiments.

A second method of calculating the dissolution rate is to use the long-term strain rate of the presented uniaxial compaction experiments in *Zhang et al.* [2010]. We have the assumption that long-term strain rate is close to the strain rate measured at the end of the experiments. We choose the test performed on analytical calcite sample flooded with calcite-saturated solution (the M13 experiment). They obtained a total strain rate of $\dot{\varepsilon} = 1 \cdot 10^{-8}\frac{1}{s}$ which, using equation (7) and average grain size value of 12 μm, can be translated to a pressure solution rate of $\dot{\xi}_2 = \dot{\varepsilon}d = 1 \cdot 10^{-8} \cdot 12 \cdot 10^{-6}$ m/s $= 1.2 \cdot 10^{-13}$ m/s.

An alternative way of estimating the dissolution rate is to use *Xu et al.*'s [2012] experiments where the dissolution flux, j_D, was measured as a function of calcite saturation. Extrapolating the data presented, we arrive to the following approximation: $j_D = 10^{-8}$ mol/m^2/s for a completely saturated solution. Using

$$\dot{\xi} = \frac{\Omega j_D}{(1 - \phi)}, \tag{15}$$

where $\Omega = 7.39 \cdot 10^{-5}$m^3/mol is the molar volume of calcite [*Michalowski and Asuero*, 2012] and $\phi = 30\%$ is the average porosity, we obtain a dissolution rate on the order of $10^{-12} - 10^{-13}$m/s, i.e., similar to the results of *Zhang et al.* [2010].

2.1.3. Upscaling to Core Scale
For a given effective stress σ_e pores larger than the critical length r_{max} participate in the fracturing process [*Japsen et al.*, 2011]. Thus, the fracture density can be written as a function of this critical length ($\rho_f(r_{max})$).

To obtain the fracture density in the direction of maximal principal stress, in the most general case one should treat the cracks as a multidimensional probability distribution: where pores are described by their size, shape, and orientation. If we assume that pores can be modeled with the same shape, the probability depends only on three variables: the size of the pore and two angles describing its orientation. The size of the pore is usually expressed as the length of the pore and presuming a uniform distribution of the orientation angles — i.e., all possible orientation is equally likely — pore size distribution is usually described by a one-dimensional density function $p(r)$ depending on characteristic pore radii. From this, the volumetric density function ($P(V)$) — the probability that a certain pore has V volume — can be obtained as

$$P(V) = \left| \frac{d}{dV}(\Gamma^{-1}(V)) \right| p(r), \tag{16}$$

where $V = \Gamma(r)$ is the volume of a pore having characteristic radius r and $\Gamma^{-1}(V)$ is its inverse function. Henceforth we assume that $\Gamma(r)$ is monotonous — i.e., pores with greater length have bigger volume — and for simplicity we denote $\Gamma(r)$ as $V(r)$.
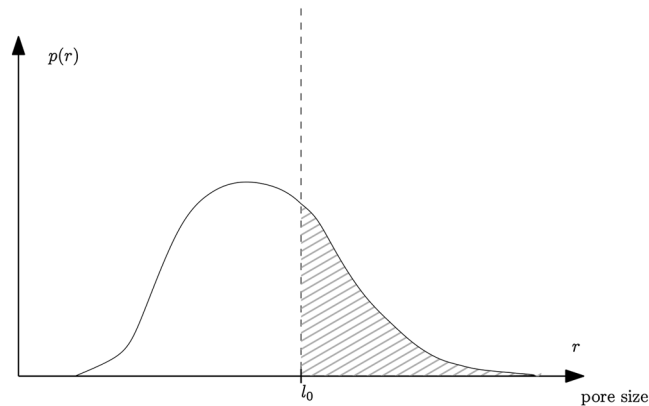
Figure 4. Probability density function of pore size. The fraction of pores bigger than a certain value r_{max} can be obtained as the integral of the density function along this length interval (i.e., $\int_{r_{max}}^{\infty} p(r)dr$) divided by the integral along the whole interval (i.e., $\int_0^{\infty} p(r)dr = 1$).

Consider a cube with characteristic length h in all dimensions with volume $V = h^3$ and porosity ϕ. Then the portion of pores longer than r_{max} is the integral of the ordinary distribution from r_{max} to infinity (Figure 4):

$$\frac{\sum_{l_i > r_{max}} l_i}{\sum l_i} = \int_{r_{max}}^{\infty} p(r)dr, \tag{17}$$

where l_i is the radius of pore i.

The volume of these pores can be calculated as the integral of the volumetric density function from $V(r_{max})$ to infinity multiplied by the total volume of pores, $V\phi$:

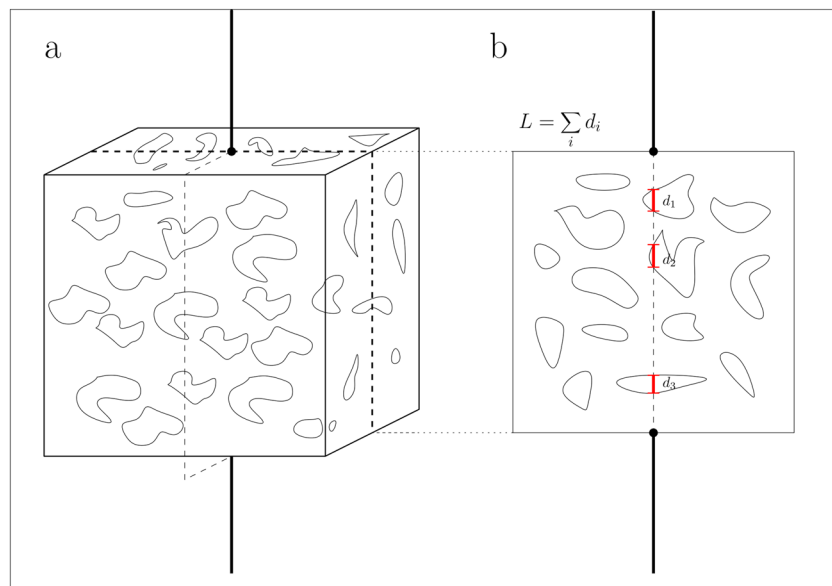$$V_{l_i > r_{max}} = V\phi \int_{V(r_{max})}^{\infty} P(V)dV. \tag{18}$$

Figure 5. The concept of average length traversed through pores of size larger than r_{max} by an arbitrary vertical line. (a) An arbitrary vertical line passing through the cube might traverse several pores. (b) This can be seen on the cross section. The length L traversed through pores of size larger than r_{max} is the sum of lengths l_i traversed through each pore. $L = \sum_i l_i$.

According to the proof in Appendix A, it is then possible to calculate the average length L traversed through pores of size larger than l by an arbitrary vertical line (Figure 5):

$$\frac{L}{h} = \frac{V_{l_i > r_{max}}}{h^3} = \frac{V\phi \int_{V(r_{max})}^{\infty} P(V)dV}{h^2}. \tag{19}$$

The number N of pores along an arbitrary line is the total length L divided by the average thickness d of pores.

$$N = \frac{L}{d}. \tag{20}$$

d can be obtained as the first moment of the pore size distribution. To calculate the fracture density, this should be divided by the total height:

$$\rho_f(r_{max}) = \frac{N}{h} = \frac{\phi}{d} \int_{V(r_{max})}^{\infty} P(V)dV. \tag{21}$$

To conclude, total strain rate can be written as

$$\dot{\varepsilon} = \rho_f(r_{max})\dot{\xi} = \frac{\phi}{d} \int_{V(r_{max})}^{\infty} P(V)dV\dot{\xi}. \tag{22}$$

Assuming that pores have a spheroidal shape with a characteristic flattening g ($g = 0$ for spheres) and their shorter radius r has Weibull distribution, the above formula can be expressed as

$$\dot{\varepsilon} = \frac{\phi\dot{\xi}}{d} \int_{V(r_{max})}^{\infty} \frac{1}{2\alpha^{1/6}} \sqrt{\frac{V}{\lambda^3}} e^{-\sqrt{\alpha\frac{V}{\lambda^3}}} dV, \tag{23}$$

where $\alpha = \frac{4}{3}\pi(1 - g)$ is the shape parameter for spheroids.

2.2. Model Parameters

If the reaction kinetics characteristic to the given rock is regarded as an internal parameter of the model, five input parameters are necessary to calculate the resulting strain during creep. The input parameters are porosity, pore size distribution, the ratio of water-wet surfaces among the new fracture surfaces, temperature, and effective stress.

The definition of temperature and porosity is rather straightforward, for maximum principal effective stress we use the relation $\sigma_e := \sigma' = \sigma_1 - p$ in our comparisons either because the Biot parameter and the plastic compressibility parameters are not known or when known they tend to be close to 1 (e.g., *Warpinski and Teufel* [1992] for Ekofisk chalk). The other parameters may be more ambiguous and hence need to be discussed.

2.2.1. Pore Size Distribution

The pore size distribution is the probability density function of pore radii. Assuming that the pore space of a rock is composed of a set of spherical pores, pore size distribution shows the abundance of the pores with different radii. Usually, little is known about the pore size distribution of a certain rock sample if it is not measured with tomography, optical or scanning electron microscopy, or with mercury injection method.

In this article we are using a Weibull distribution to represent the one-dimensional pore size distribution with shape parameter $k = 1.5$ and a scale parameter λ:

$$p(r) = \frac{1.5}{\lambda} \sqrt{\frac{r}{\lambda}} \cdot e^{-(r/\lambda)^{1.5}}; \tag{24}$$

the volumetric density function—sometimes referred to as exponentiated Weibull distribution—has the following form:

$$P(V) = \frac{3\pi}{8} \sqrt{\frac{r^3}{\lambda^3}} e^{-\sqrt{\frac{4\pi}{3}\frac{r^3}{\lambda^3}}}. \tag{25}$$
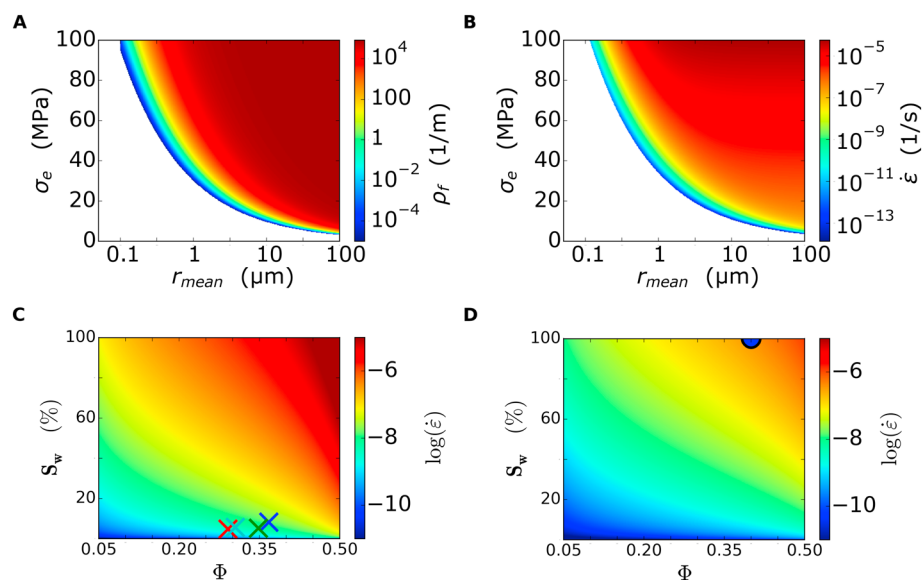
Figure 6. Model calculations of (a) fracture density and (b–d) strain rate values as a function of mean pore size, effective stress, porosity, and water saturation using a Weibull-type pore size distribution with shape parameter 0.5. In Figures 6a and 6b calculations $\phi = 0.37$ porosity, and 5% water saturation level was used and in Figures 6c and 6d $r_{mean} = 2.2$ μm and $\sigma_e = 35$ MPa and 6.3 MPa were used. The crosses in Figure 6c correspond to the effective stress and water saturation conditions used in *Omdal et al.* [2010] experiments, while the half-circle in Figure 6d indicate the states of the second and third phases of experiment K14 shown in the Table 2.

This volumetric density function is biased toward lower values compared to the pore radius density function: having lower values more probable than the original Weibull density function. The density function also deviates at greater values from normal density function having longer lag toward greater values.

This distribution function adequately described pore size distribution measurements performed on North Sea chalk [*Japsen et al.*, 2011]. Using the above distribution as an input parameter, our model can be used to predict the compaction history of the producing Ekofisk field [*Keszthelyi et al.*, 2016].

2.2.2. The Ratio of Water-Wet Surfaces

For pressure solution to take place the presence of water inside the new fractures is necessary. However, the pore fluid inside a rock is sometimes a mixture of non-miscible fluids (e.g., oil and water), one of which usually wets the pore walls. To predict which fluid will enter a newly created fracture is thus a complex question. As a first-order estimation we consider that the rate of pressure solution is a linear function of the water saturation, assuming that the probability that water entering the newly created fractures is proportional to the relative amount of water available in the pore space. Therefore, we multiply all fracture density data with an average water saturation which is given for each sample.

3. Results

First we will show some general results to display the characteristics of the model and then we will compare model predictions with experimental and field data. Results of model calculations of fracture density and strain rate for a large range of stresses, mean pore size, porosity and water saturation with material parameters for calcite are shown in 6.

Figures 6a and 6b show that both fracture density and strain rate vary rapidly in a relatively narrow band of effective stress and mean pore values; that is, they are nonlinear functions of mean pore size and stress. Thus, the dominating mechanism determining the strain rate in this model is the fracture density. However, even if the strong effective stress dependence is due to the nature of fracturing, the strain rates are produced by the pressure solution on the fracture surfaces and pressure solution rate varies with stress and pore size independently of the fracture density.
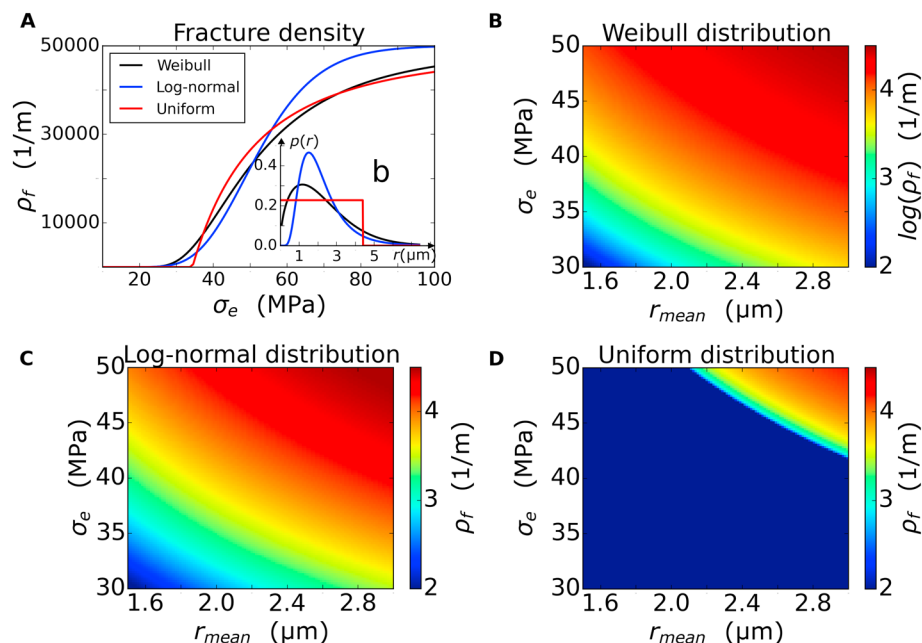
Figure 7. Fracture density as a function of the probability distribution function and effective stress while porosity is kept at $\phi = 0.25$. (a) The fracture density as a function of effective stress for three pore size distributions (see insert) having the same mean at ($r_{mean} = 2.2$ μm) but from different families of distribution functions. The variations of fracture densities (color coded) as a function of mean pore size and effective stress inside a family of pore size distribution functions are shown (b) for Weibull-type distributions with shape parameter 1.5, (c) for lognormal distributions, and (d) for uniform distributions.

Figures 6c and 6d show the variation in predicted strain with porosity and water saturation for a given porosity distribution and stress. The dependence on water saturation (see equations (4) and (6)) is nearly linear, and a change in S_w from 0.1 to 1 changes the strain rate by 2 orders of magnitude.

According to equation (22), the overall strain rate is a function of porosity, mean pore size, and water saturation and an integral of the pore size distribution in the region larger than a critical threshold. The lower the stress, the higher the threshold value is from which the integral is calculated. Since usually only a small number of large pores are present in rocks, the pore size distribution tends to have small values toward the higher end. Therefore, to obtain good predictions at lower stresses, it is essential to have detailed constraints on the tail of the pore size distribution, as already a small error in the abundance of large pores may result in large

Table 2. Comparison of Strain Rates From the Experimental Data of *Omdal et al.* [2010] and *Hellmann et al.* [2002a] to Our Model Predictions[a]

	Omdal et al. [2010]				*Hellmann et al.* [2002a]		
	K14	R26	SKS13	SKS20	First Phase	Second Phase	Third Phase
Porosity (%)	36.75	34.8	29.1	30.5	40	40	40
Water saturation (%)	8.25	5.21	4.78	5.64	100	100	100
σ_1 (MPa)	44.2	46.9	45.0	44.2	4.0	7.0	7.0
σ_3 (MPa)	19.5	11.5	17.0	15.5	4.0	4.0	4.0
Pore pressure (MPa)	9.0	9.0	9.0	9.0	0.3	0.3	0.3
Temperature (K)	368	368	368	368	298	298	323
Measured long-term strain rate (s^{-1})	$5.0 \cdot 10^{-9}$	$7.9 \cdot 10^{-9}$	$7.5 \cdot 10^{-9}$	$4.0 \cdot 10^{-9}$	$3.5 \cdot 10^{-10}$	$1.2 \cdot 10^{-9}$	$1.4 \cdot 10^{-9}$
Predicted strain rate (s^{-1})	$5.8 \cdot 10^{-9}$	$6.3 \cdot 10^{-9}$	$1.4 \cdot 10^{-9}$	$1.5 \cdot 10^{-9}$	$1 \cdot 10^{-10}$	$2.7 \cdot 10^{-9}$	$1.7 \cdot 10^{-9}$
$\dot{\varepsilon}_{predicted}/\dot{\varepsilon}_{measured}$	1.16	0.79	0.19	0.38	0.29	2.25	1.21
Error: $\left\lvert \dot{\varepsilon}_{predicted} - \dot{\varepsilon}_{measured} \right\rvert / \dot{\varepsilon}_{measured}$	0.16	0.20	0.81	0.63	0.71	1.25	0.21

[a]Parameters needed for the model are shown in the table; pore size distribution was chosen to be Weibull distribution with 2.2 μm in the case of *Omdal et al.* [2010], while the measured pore size distribution were used in the case of *Hellmann et al.* [2002a].
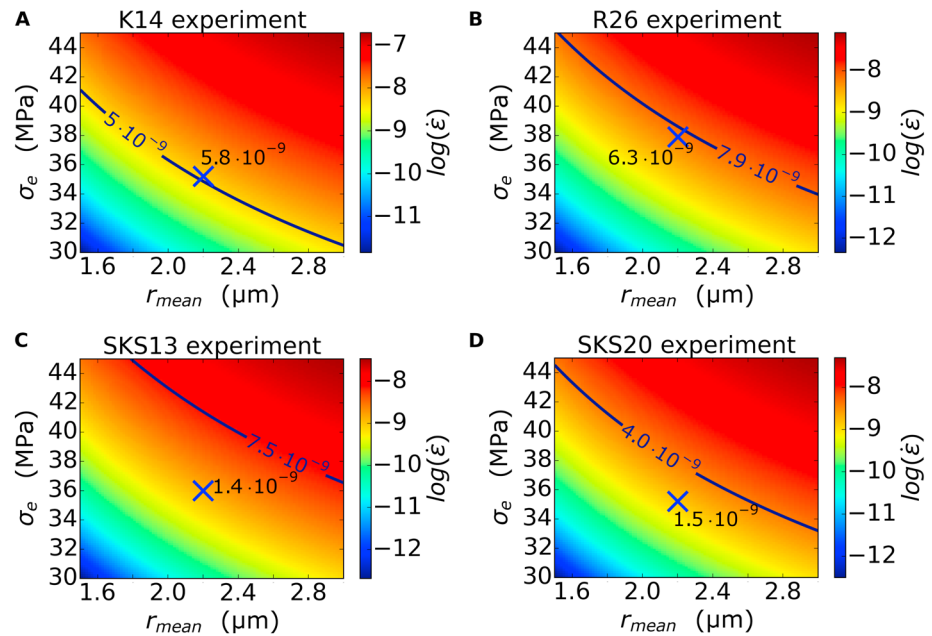
Figure 8. Predicted strain rates as function of mean pore size and effective stress at conditions of each *Omdal et al.* [2010] experiments: for all predictions Weibull-type distribution with shape parameters 1.5 and pressure solution parameters listed in Table 1, the water saturation and porosity are different in each subplot: (a) $S_w = 8.25\%$, $\phi = 36.75\%$; (b) $S_w = 5.21\%$, $\phi = 34.8\%$; (c) $S_w = 4.78\%$, $\phi = 29.1\%$; and (d) $S_w = 5.64\%$, $\phi = 30.5\%$. In all plots the cross represents the strain rate predicted by the model at the effective stress value used in the experiments. The solid lines of constant strain rate equals the strain rates of the experiments after 10 days of creeping. The slight changes in the color between plots are due to the porosity and water saturation level changes.

error in the predicted strain rate. Figure 7 illustrates the effects of the large pore tails for different pore size distributions around the same mean pore size. While the pore size distributions (shown in Figure 7a) resemble each other, the predicted fracture densities (shown in Figures 7b–7d) vary significantly. This is most visible if the Weibull distribution (Figure 7b) is compared with a uniform distribution (Figure 7d). Higher fracture density values are observed in the case of Weibull distribution as the uniform distribution (especially if the mean pore size is small) lacks sufficiently large pores to initiate fracturing.

To test the model, we compare model predictions with existing creep experiment data on wet carbonate samples. The theoretical model predictions displayed in Table 2 and Figures 8–10 use no extra parameters to fit the data.
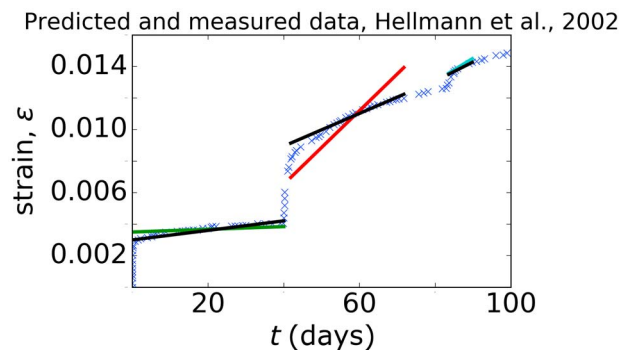

Figure 9. Deformation curves of experiment L9-11 shown in *Hellmann et al.* [2002a], data reproduced by digitizing the original figures. In this experiment they initially applied 4 MPa maximal principal stress (phase 1), then increased it to 7 MPa (phase 2). In the next step they increased temperature from 298 K to 323 K (phase 3) and then started to inject saline solution (phase 4). The colored straight lines show the predicted strain rates. The elastic strain and the time dependence of the strain rate are not part of our model. Therefore, the straight lines should be compared to the strain rates after 10 days of the experiment (indicated by black lines).
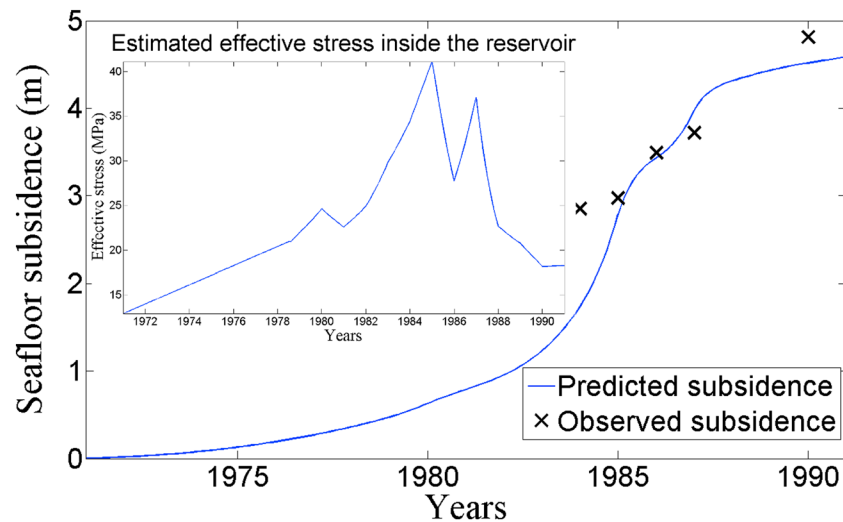
Figure 10. Estimated subsidence of the Ekofisk field compared to field observations between 1971 and 1990. Average reservoir parameters are used to make the following predictions: porosity $\phi = 37.5\%$, water saturation $S_w = 4.5\%$, pore size distribution is a Weibull distribution with shape parameter 1.5, and mean pore size $r_{max} = 2.2$ μm. Pressure history data calculated from production data are used for the predictions and are presented in the insert. Modified from *Keszthelyi et al.* [2016].

We consider the experiments of *Omdal et al.* [2010] and *Hellmann et al.* [2002a] which were conducted for chalk with different porosity distributions, using very different water saturation and effective stress conditions (see marks in Figures 6c and 6d). *Omdal et al.* [2010] analyzed chalk samples from different locations: six from outcrop at Stevns Klint, Denmark, three Kansas chalk, and two reservoir samples from the North Sea. They applied gradually decreasing pore pressure in a uniaxial compaction configuration, and in the final state they let samples creep. The Stevns Klint samples had a very large porosity change prior to the creep phase of the experiments; therefore, the initial porosity values we have used in the calculations were corrected to the changes during the depletion phase. Due to the fact that experiments on two Kansas chalk samples and one reservoir chalk were terminated too early for long-term strain rates to be read from the diagram, these experiments were omitted from our comparison. The remaining cores were used to make our comparison, with the results of our prediction for the K14 outcrop, the R26 reservoir, and two representative samples from the Stevns Klint (SKS13 and SKS20) shown in Table 2.

Since *Omdal et al.* [2010] did not publish the pore size distribution of their samples, we have used literature data: the same Weibull pore size distribution with a mean of 2.2 μm as reported in *Japsen et al.* [2011] for some North Sea chalk samples assuming that the depositional conditions of the samples were similar. As displayed in Figure 6, our model is very sensitive to the pore size distribution and the lack of such information makes this a test of the usability of a generic pore size distribution in the model. The long-term strain rates—the strain rate at the end of the longest lasting experiments—were read from *Omdal et al.* [2010], and by knowing the initial porosity, water saturation, and effective stress (using the $\sigma_e = \sigma_1 - p$ formulation), it was possible to calculate the predicted strain rates using our model. Table 2 shows the predicted (pressure solution controlled) stain rates along with the measured strain rates of *Omdal et al.* [2010] with a reasonable agreement between the two rates. Predicted strain rates for a range of mean pore size and effective stress values are plotted for all experiments and compared to measured strain rates in Figure 8.

Hellmann et al. [2002a] performed triaxial tests on chalk samples from the Paris basin with horizontal stresses being kept constant and with fluid pressures kept below 0.3 MPa.

We consider experiment L9-11 where they initially applied smaller confining stresses, then increased it to 7 MPa. In the next step they increased the temperature from 298 K to 323 K before injecting saline solution. We calculated the measured strain rate as the slope of the strain versus time plot [*Hellmann et al.*, 2002a, Figure 9] around 10–20 days after the start of each experiment step (similar timescale as in *Omdal et al.* [2010]).

Hellmann et al. [2002b] showed pore size distributions for the samples used in the experiments. They performed mercury injection measurements. Using these pore size distributions as input parameter results in accurate strain rate predictions, as can be seen in Table 2. The porosity is kept at 40%, while the water saturation is 1. Deformation curves of the experiments compared with the constant strain rate predicted by the model are shown in Figure 9. Our current model has no time dependence of the strain rate, whereas in reality the compaction experiments of *Hellmann et al.* [2002a] show considerable work hardening which should be included in future models.

The summary of sample properties, experimental conditions, measured strain rates, and calculated strain rates, as well as the ratio of these two strain rates, are in Table 2. All the predictions are of the right order of magnitude.

The compaction history of the Ekofisk field, a carbonate reservoir, was also used to test our model. During the initial phase of oil production the reservoir pressure was considerably reduced (i.e., the effective stress increased) and significant seafloor subsidence was observed (almost 5 m from 1971 to 1989) due to compaction of the reservoir rocks.

We assume that compaction is homogenous within the reservoir and controlled by effective stress changes and use fluid pressures (see insert in Figure 10) calculated from the production data to make predictions based on our model. The details of the calculation are presented in *Keszthelyi et al.* [2016]. The porosity and water saturation is taken to be equal to the average reservoir values (i.e., $\phi = 37.5\%$ and $S_w = 4.5\%$), while we use the same pore size distribution as in our predictions for *Omdal et al.*'s [2010] experiments (i.e., a Weibull distribution with shape parameter 1.5 and mean pore size $r_{max} = 2.2$ μm). Figure 10 shows that the predictions agree well with the observations from the Ekofisk field.

The pore size distribution data presented in *Hellmann et al.* [2002b] could be digitized only with large uncertainty, and hence, the strain rate predictions are also associated with large uncertainties (which for small stresses can be as high as an order of magnitude). This is most remarkable in the first phase of the *Hellmann et al.*'s [2002a] experiment where the effective stress is very low. The later phases, with larger effective stress, give a good agreement with the measured strain rates. Having more reliable data on pore size distribution will result in predictions with smaller uncertainties.

Another source of uncertainty is the choice of pressure solution model and the associated variables. While some of the variables can be determined with larger confidence, two key parameters (the rate coefficients for precipitation k_p and the diffusion product DCS) are usually poorly constrained, partly because of measurement errors and partly because these parameters are very sensitive to the exact composition of the pore fluid and the solid. In our model, the strain rate is a linear function of these variables. However, an error of more than an order of magnitude in the predicted strain rates is possible if the chemical composition is not well known.

4. Discussion and Conclusion

Based on simple physical concepts, we were able to develop a micromechanical model of compaction creep which combines microscopic fracturing and pressure solution and which upscaled to macroscopic scale through the concept of fracture density, is able both to reproduce the magnitude of strain rates observed in creep experiments of (partly) water-filled carbonate samples and to accurately predict the subsidence of a producing reservoir.

The model is different from previous micromechanical models [e.g., *Ashby and Sammis*, 1990; *Brantut et al.*, 2012, 2013, 2014] in three aspects.

1. It does not use any exact solution of fracture mechanics.
2. It does not assume any specific pore configuration but treats the pore space in a general sense: as a collection of pores having a measurable pore size distribution. This distribution is then used as an input parameter for the model.
3. It does not use parameters or functions derived from empirical deformation tests on the material in question.

Furthermore, the mentioned models assume that the strain originates from subcritical crack growth, related stress corrosion, or cataclastic pore collapse. In our model, the strain is mainly due to pressure solution.

The reason for this is that fracturing in carbonates is eased significantly in the presence of water and dissolution of calcite is accelerated on fresh fracture surfaces.

With these significant differences from previous models our model gives good agreement with observed strain rates. The discrepancy between model predictions and observations may be due to uncertainties of input parameters and the parameters used for the pressure solution description. Among the input parameters, an accurate description of the pore size distribution is very important. Of particular importance is the tail of this distribution since large variation in strain rate may be observed for systems with similar average pore size. A large uncertainty in input parameters may come from the pore size distribution. The model uses an integral of the distribution over the largest pores; therefore, to get a correct estimation of the strain rate, it is critical to know the pore size distribution of the largest pores with high accuracy.

Another uncertainty is connected to the mechanics of fracturing. In our model we modeled pore volumes as distinct elliptical holes in the rock. As the pore space is a mostly interconnected volume with a complex shape, this very simple model of pore space gives a good prediction to strain rates.

Currently, our model is applied only to carbonates; however, by modifying the pressure solution description in the model by introducing precipitation and diffusion rates relevant for quartz, it may also predict creep strain rates in siliciclastic rocks. Since pressure solution rates are much slower in quartz, strains from poroelastic effects and from mechanical effects associated with subcritical crack growth may also have an important contribution to the total strain. A siliciclastic analogue to the producing field of the North Sea is the Groningen field in the Netherlands where gas is produced from a sandstone reservoir. The amplitude of the subsidence in the Groningen field is 1 order of magnitude smaller than for the Ekofisk field. Accounting for the lower dissolution rate of silicates, it is possible that pressure solution triggered by microscopic fracturing is an important mechanism also in that case.

Microstructural analysis of compacted carbonate samples could give further validation of our model. A study by *Nermoen et al.* [2015] carried out on samples compacted in a brine-saturated environment shows considerable reworking of the microstructures due to chemical alterations during the compaction. This experimental result supports the idea that microscopic fracturing-triggered pressure solution is an underlying mechanism of carbonates compaction.

Appendix A: Proof for the Upscaling

Let us consider a cube with only one pore (see Figure A1). For simplicity we consider a spheroidal pore with a rotational axis parallel to x (the demonstration is similar to more complex-shaped pore) while its center is located at (x_0, y_0, z_0) point. A spheroid has a circular cross section within the z_0 plain; its diameter is R. The flattening of the spheroid is g. $\lambda(x, y)$, a function showing the length traversed at a certain (x, y) position and L: the average length traversed through pore space by an arbitrary line is the expected value of $\lambda(x, y)$. In this particular case $\lambda(x, y)$ can be expressed as

$$\lambda(x,y) = \begin{cases} 2 \cdot (R - R \cdot g) \sqrt{1 - \frac{(x-x_0)^2 + (y-y_0)^2}{R^2}} \\ \qquad \text{if} \quad |x - x_0| < \frac{R}{2}, \quad |y - y_0| < \frac{R}{2} \\ 0 \qquad \text{otherwise} \end{cases} \tag{A1}$$

The expected value of $\lambda(x, y)$ is thus

$$E\left[\lambda(x,y)\right] = \int_0^h \int_0^h \lambda(x,y) \cdot p(x,y) \cdot \mathrm{d}x\mathrm{d}y = \int_0^h \int_0^h \lambda(x,y) \cdot \frac{1}{h^2} \cdot \mathrm{d}x\mathrm{d}y = \frac{1}{h^2} \cdot \int_0^h \int_0^h \lambda(x,y) \cdot \mathrm{d}x\mathrm{d}y. \tag{A2}$$

In this particular case

$$E\left[\lambda(x,y)\right] = \frac{1}{h^2} \int_{x_0-\frac{R}{2}}^{x_0+\frac{R}{2}} \int_{y_0-\frac{R}{2}}^{y_0+\frac{R}{2}} 2(R - Rg) \sqrt{1 - \frac{(x-x_0)^2 + (y-y_0)^2}{R^2}} \mathrm{d}x\mathrm{d}y = \frac{1}{h^2} \cdot \frac{4}{3}\pi R^2 (R - Rg) = \frac{1}{h^2} \cdot V_{\text{pore}}. \tag{A3}$$
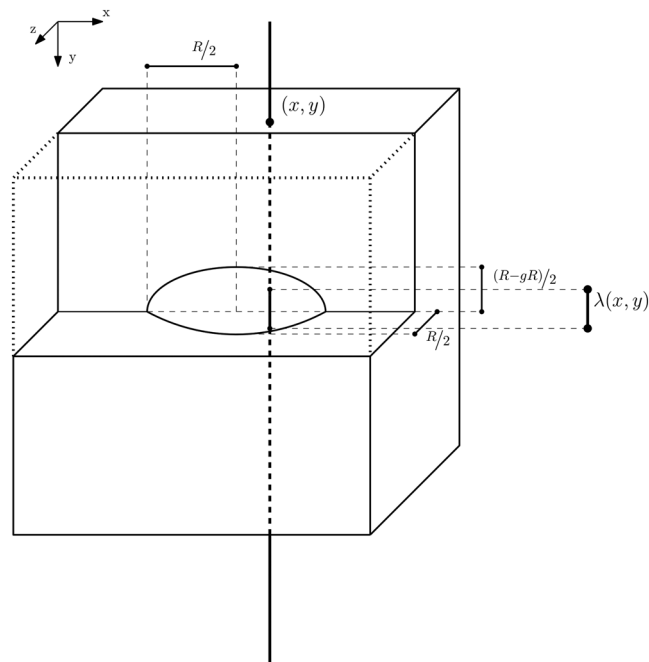
Figure A1. A cube with one elliptical pore. The pore has a diameter of R in both x and y directions and has a flattening g. The arbitrary vertical line is at (x, y) position and indicated by a thick dashed line. The section within the spheroid is shown by a continuous line and has a length $\lambda(x, y)$. The average length traversed through pores is then the expected value of this function.

The last relation also applies for other more complex-shaped objects thus the average length traversed through pores by an arbitrary vertical line

$$L = E\left[\lambda(x, y)\right] = \frac{1}{h^2} \cdot V_{\text{pore}}. \tag{A4}$$

Appendix B: Table of Variables

We provided a table of all variables used in the Article to ease the readability:

Table B1. List of Variables Used in the Article

	Variable Description
A_c	geometric constant of diffusion
A_p	geometric constant of precipitation
B	dimensionless constant of the precipitation
C	solubility of the solid
d	average pore diameter/thickness, taken equal to average diffusion distance
D	diffusivity of ions within grain boundary fluid
$E(\ldots)$	expected value
F	grain shape factor
g	flattening of spheroid
G	energy release rate
h	characteristic length scale
j_D	flux of dissolution
k_p	rate coefficient for precipitation
K	bulk modulus of the matrix
$l = r_{\max}$	critical pore radius
L	average length traversed through pore space by an arbitrary vertical line

Table B1. (continued)

Variable	Description
M	dimensionless constant of the diffusion
N	number of pores
p	pore fluid pressure
$p(r)$	probability density function of pore size distribution
$P(V)$	density function of volumetric pore size distribution
q	geometric constant
r	pore radius
$r_{max} = l$	critical pore radius
R	universal gas constant
S	mean thickness of boundary fluid film
S_w	water saturation
t	time
T	temperature
U_E	elastic energy stored
U_s	surface energy released
Z	coordination number
α	shape parameter for spheroids
β	geometric constant
γ_s	surface energy of the solid
$\dot{\varepsilon}$	strain rate
λ	scale parameter of Weibull distribution
$\lambda(x, y)$	length traversed through pores by a vertical line with (x, y) horizontal coordinates
μ	pore fluid viscosity
ϕ	porosity
ρ	pore fluid density
ρ_f	fracture density
σ	(vertical) confining stress
$\sigma' = \sigma_e$	effective stress
$\dot{\xi}$	pressure dissolution rate
$\dot{\xi}_p$	pressure dissolution rate controlled by precipitation
$\dot{\xi}_d$	pressure dissolution rate controlled by diffusion
Ω	molar volume of calcite

References

Andrade, E. D. C. (1910), On the viscous flow in metals, and allied phenomena, *Proc. R. Soc. A*, *84*(567), 1–12.

Ashby, M., and C. Sammis (1990), The damage mechanics of brittle solids in compression, *Pure Appl. Geophys.*, *133*(3), 489–521.

Bos, B., C. J. Peach, and C. J. Spiers (2000), Frictional-viscous flow of simulated fault gouge caused by the combined effects of phyllosilicates and pressure solution, *Tectonophysics*, *327*(3), 173–194.

Brantut, N., P. Baud, M. J. Heap, and P. G. Meredith (2012), Micromechanics of brittle creep in rocks, *J. Geophys. Res.*, *117*, B08412, doi:10.1029/2012JB009299.

Brantut, N., M. J. Heap, P. G. Meredith, and P. Baud (2013), Time-dependent cracking and brittle creep in crustal rocks: A review, *J. Struct. Geol.*, *52*, 17–43.

Brantut, N., M. J. Heap, P. Baud, and P. G. Meredith (2014), Mechanisms of time-dependent deformation in porous limestone, *J. Geophys. Res. Solid Earth*, *119*, 5444–5463, doi:10.1002/2014JB011186.

Carter, N. L., and S. H. Kirby (1978), Transient creep and semibrittle behavior of crystalline rocks, *Pure Appl. Geophys.*, *116*, 807–839.

Croize, D., F. Renard, and J. P. Gratier (2013), Compaction and porosity reduction in carbonates: A review of observations, theory, and experiments, *Adv. Geophys.*, *54*, 181–238.

Feazel, C. T. (1988), Chalk from the Ekofisk area, North Sea: Nannofossils + micropores = giant fields, in *Giant Oil and Gas Fields*, vol. 12, pp. 155–178, Soc. Econ. Paleont. Mineralogists, Spec. Publ. of SEPM, Houston, Tex.

Gratier, J. P., F. Renard, and P. Labaume (1999), How pressure solution creep and fracturing processes interact in the upper crust to make it behave in both a brittle and viscous manner, *J. Struct. Geol.*, *21*(8), 1189–1197.

Gratier, J.-P., F. Renard, and D. K. Dysthe (2013), The role of pressure solution creep in the ductility of the Earth's upper crust, *Adv. Geophys.*, *54*, 47–179.

Griffith, A. A. (1921), The phenomena of rupture and flow in solids, *Philos. Trans. R. Soc. A*, *221*, 163–198.

Griggs, D. T. (1936), Deformation of rocks under high confining pressures: I. Experiments at room temperature, *J. Geol.*, *44*, 541–577.

Hassenkam, T., L. Skovbjerg, and S. Stipp (2009), Probing the intrinsically oil-wet surfaces of pores in North Sea chalk at subpore resolution, *Proc. Natl. Acad. Sci.*, *106*(15), 6071–6076.

Hassenkam, T., A. Johnsson, K. Bechgaard, and S. L. S. Stipp (2011), Tracking single coccolith dissolution with picogram resolution and implications for CO$_2$ sequestration and ocean acidification, *Proc. Natl. Acad. Sci.*, *108*(21), 8571–8576.

Hellmann, R., P. J. N. Renders, J.-P. Gratier, and R. Guiguet (2002a), Experimental pressure solution compaction of chalk in aqueous solutions. Part 1. Deformation behavior and chemistry, in *Water-rock Interaction, Ore Deposits, and Environmental Geochemistry: A tribute to David A. Crerar*, vol. 7, edited by R. Hellmann and S. A. Wood, pp. 129–152, Geochem. Soc. Spec. Publ., Washington, D. C.

Hellmann, R., P. Gaviglio, P. J. N. Renders, J. P. Gratier, S. Bekri, and P. Adler (2002b), Experimental pressure solution of chalk in aqueous solutions. Part 2. Deformation examined by SEM, porosimetry, synthetic permeability, and X-ray computerized tomography, in *Water–Rock Interactions, Ore Deposits, and Environmental Geochemistry: A Tribute to David A. Crerar*, vol. 7, edited by R. Hellman and S. A. Wood, pp. 153–176, Geochem. Soc. Spec. Publ., Washington, D. C.

Hickman, S. H., and B. Evans (1995), Kinetics of pressure solution at halite-silica interfaces and intergranular clay films, *J. Geophys. Res.*, *100*(B7), 13,113–13,132.

Irwin, G. R. (1958), *Handbuch der Physik*, vol. 6, chap. Fracture, pp. 551–590, Springer, Berlin.

Japsen, P., D. Dysthe, E. Hartz, S. Stipp, V. Yarushina, and B. Jamtveit (2011), A compaction front in North Sea chalk, *J. Geophys. Res.*, *116*, B11208, doi:10.1029/2011JB008564.

Keszthelyi, D., D. K. Dysthe, and B. Jamtveit (2016), Compaction of North-sea chalk by pore-failure and pressure solution in a producing reservoir, *Frontiers Phys.*, *4*, 4.

Lawn, B. (1993), *Fracture of Brittle Solids*, Cambridge Univ. Press, Cambridge, U. K.

Michalowski, T., and A. Asuero (2012), Thermodynamic modelling of dolomite behavior in aqueous media, *J. Thermodyn.*, *2012*, 723052.

Moore, C. H. (1989), *Carbonate Diagenesis and Porosity*, vol. 46, Elsevier, Amsterdam, Netherlands.

Nermoen, A., R. I. Korsnes, A. Hiorth, and M. V. Madland (2015), Porosity and permeability development in compacting chalks during flooding of nonequilibrium brines: Insights from long-term experiment, *J. Geophys. Res. Solid Earth*, *120*, 2935–2960, doi:10.1002/2014JB011631.

Omdal, E., M. V. Madland, T. G. Kristiansen, N. B. Nagel, R. I. Korsnes, and A. Hiorth (2010), Deformation behavior of chalk studied close to in situ reservoir conditions, *Rock Mech. Rock Eng.*, *43*(5), 557–580.

Phillips, P. (1905), XLIX. The slow stretch in indiarubber, glass, and metal wires when subjected to a constant pull, *Philos. Mag. J. Sci.*, *9*(52), 513–531.

Pluymakers, A. M. H., C. Spiers, and C. Peach (2014), Compaction creep of simulated anhydrite fault gouge by pressure solution: Theory v. Experiments and implications for fault sealing, in *Rock Deformation from Field, Experiments and Theory: A Volume in Honour of Ernie Rutter*, vol. 409, pp. 107–124, Geol. Soc. Spec. Publ., London.

Renard, F., A. Park, P. Ortoleva, and J. P. Gratier (1999), An integrated model for transitional pressure solution in sandstones, *Tectonophysics*, *312*(2), 97–115.

Røyne, A., J. Bisschop, and D. K. Dysthe (2011), Experimental investigation of surface energy and subcritical crack growth in calcite, *J. Geophys. Res.*, *116*, B04204, doi:10.1029/2010JB008033.

Schutjens, P. M. T. M., T. H. Hanssen, M. H. H. Hettema, J. Merour, P. De Bree, J. W. A. Coremans, and G. Helliesen (2004), Compaction-induced porosity/permeability reduction in sandstone reservoirs: Data and model for elasticity-dominated deformation, *SPE Reservoir Eval. Eng.*, *7*(03), 202–216.

Terzaghi, K. (1943), Theory of Consolidation, in *Theoretical Soil Mechanics*, pp. 265–296, John Wiley, Hoboken, N. J., doi:10.1002/9780470172766.ch13.

Vajdova, V., P. Baud, L. Wu, and T. F. Wong (2012), Micromechanics of inelastic compaction in two allochemical limestones, *J. Struct. Geol.*, *43*, 100–117.

Warpinski, N., and L. Teufel (1992), Determination of the effective stress law for permeability and deformation in low-permeability rocks, *SPE Form. Eval.*, *7*(2), 123–131.

Xu, J., C. Fan, and H. H. Teng (2012), Calcite dissolution kinetics in view of Gibbs free energy, dislocation density, and pCO$_2$, *Chem. Geol.*, *322-323*, 11–18.

Zhang, X., C. Spiers, and C. Peach (2010), Compaction creep of wet granular calcite by pressure solution at 28°C to 150°C, *J. Geophys. Res.*, *115*, B09217, doi:10.1029/2008JB005853.

Zhu, W., P. Baud, and T. F. Wong (2010), Micromechanics of cataclastic pore collapse in limestone, *J. Geophys. Res.*, *115*, B04405, doi:10.1029/2009JB006610.